A Simulation of the Nuclear High-Altitude Electromagnetic Pulse (HEMP) Produced by the X-Ray in the Ionosphere

Article *in* Journal of Geophysical Research: Space Physics · November 2021

DOI: 10.1029/2021JA029533

CITATIONS
2

READS
165

5 authors, including:

Jiansheng Yao
Institute of Applied Physics and Computational Mathematics
15 PUBLICATIONS **34** CITATIONS
SEE PROFILE

Yingkui Zhao
Institute of Applied Physics and Computational Mathematics
10 PUBLICATIONS **50** CITATIONS
SEE PROFILE

Hantian Zhang
Institute of Applied Physics and Computational Mathematics
25 PUBLICATIONS **94** CITATIONS
SEE PROFILE

Sun Jicheng
Polar Research Institute of China
25 PUBLICATIONS **184** CITATIONS
SEE PROFILE

JGR Space Physics

RESEARCH ARTICLE
10.1029/2021JA029533

Key Points:

- The ignored electromagnetic component in previous studies should be considered
- The "newly born" secondary electrons deviate from the drifting Maxwellian distribution; thus, it cannot be described with the "swarm theory"
- The widely accepted assumption that primary electrons move forward is invalid to study the X-ray-produced high-altitude electromagnetic pulse

Correspondence to:
J. Yao and Y. Zhao,
ab135794@mail.ustc.edu.cn;
zhao_yingkui@iapcm.ac.cn

Citation:
Yao, J., Zhao, Y., Ye, D., Zhang, H., & Sun, J. (2021). A simulation of the nuclear high-altitude electromagnetic pulse (HEMP) produced by the X-ray in the ionosphere. *Journal of Geophysical Research: Space Physics*, *126*, e2021JA029533. https://doi.org/10.1029/2021JA029533

Received 20 MAY 2021
Accepted 30 SEP 2021

A Simulation of the Nuclear High-Altitude Electromagnetic Pulse (HEMP) Produced by the X-Ray in the Ionosphere

Jiansheng Yao[1,2], Yingkui Zhao[1], Difa Ye[1], Hantian Zhang[1], and Jicheng Sun[3]

[1]Institute of Applied Physics and Computational Mathematics, Beijing, China, [2]CAS Key Lab of Geospace Environment, School of Earth and Space Sciences, University of Science and Technology of China, Hefei, China, [3]MNR Key Laboratory for Polar Science, Polar Research Institute of China, Shanghai, China

Abstract Since the 1960s, scientists have been studying the nuclear high-altitude electromagnetic pulse (HEMP) produced by γ-rays. However, the HEMP produced by X-rays in the ionosphere has rarely been studied by previous studies. In this study, we investigate this issue via a 1-D particle-in-cell/Monte Carlo (PIC/MC) simulation model. We find that the amplitude of the electrostatic component quickly increases to the peak, and then decreases gradually. The amplitude of the electromagnetic field component gradually increases and exceeds the amplitude of the electrostatic field. This phenomenon, which contradicts previous hypotheses, adds to our understanding of the X-ray-produced HEMP. The evolution of secondary electrons formed by photoelectrons through ionization is very intriguing: the "newly born" secondary electrons deviate from the drifting Maxwellian distribution; thus, they cannot be described with the "swarm theory" which is based on the assumption that electrons satisfy a drifting Maxwellian distribution. This result is consistent with the recent experiment. In addition, our research indicates that assuming that all photoelectrons go forward considerably increases the amplitude of electric fields, making secondary electrons take longer to reach equilibrium. This widely used assumption in previous studies of the γ-ray-produced HEMP is invalid to study the X-ray-produced HEMP.

Plain Language Summary This is the first particle-in-cell/Monte Carlo collision simulation work of the high-altitude electromagnetic pulse produced by X-rays.

1. Introduction

Since the 1960s, scientists have found that the nuclear explosion was a strong source of the electromagnetic pulse (e.g., Berthold et al., 1960; Bomke et al., 1960, 1964; Casaverde et al., 1963; Cotterman, 1965; Crook et al., 1963; Dinger & Garner, 1963; Field & Greifinger, 1967; Latter & LeLevier, 1963; Wittwer et al., 1974). The majority of previous studies on HEMP have used γ-rays rather than X-rays as the energy source (e.g., Leuthiiuser, 1992; Li et al., 2020; Longmire, 1978; Meng, 2013; Roussel-Dupré, 2017; Zhang & Zhang, 2018). This is appropriate for observers situated below 40 km in altitude (Higgins et al., 1973; Karzas & Latter, 1965; Price, 1974), because X-rays have been absorbed within several tens of meters from the burst, thus only energetic γ-rays with several kilometers free path can proceed at low altitudes. In general, the absorption region of γ-rays is between 20-km and 40-km altitudes (Karzas & Latter, 1965; Maraschi & Cavaliere, 1977), where γ-rays produce a significant amount of free electrons that screen electrical effects caused by the X-ray (Higgins et al., 1973). As a result, when studying the EMP below 30 km, only γ-rays need to be considered.

However, when we research the impact of HEMP on the ionosphere at altitudes greater than 60 km, X-rays will play the dominant role. Since X-rays have a higher density than γ-rays by a factor of $10^4 - 10^5$ at altitudes of 50–100 km (Higgins et al., 1973), and X-rays are strongly absorbed within this layer. Therefore, the number density of photoelectrons produced by X-rays is much greater than that of Compton electrons produced by γ-rays. As a result, when studying the HEMP generated in the ionosphere's D-region (at the altitude of 60–90 km), we only consider photoelectrons produced by X-rays. The basic physical mechanism of nuclear HEMP generated by X-rays is similar to that of the EMP produced by γ-rays (Karzas & Latter, 1965; Longmire, 1978): X-rays generate photoelectrons by photoionizing air molecules, and photoelectrons deflected by the geomagnetic field constitute the primary current, which causes the EMP. As photoelectrons ionize air molecules, they can also generate a significant amount of secondary electrons. Secondary electrons

multiply as well due to cascading ionization. Secondary electrons are moved by the electric field and form the secondary electron current, which has the opposite orientation to the primary current and hence neutralizes it. After that, the EMP would eventually achieve equilibrium.

During 1950s–1970s, the Soviet Union and the United States conducted many high-altitude nuclear experiments (e.g., Hess, 1964; Hoerlin, 1976; Jones et al., 1982; Zak, 2006), of which the Starfish Prime on 1962 was the direct experiment on HEMP, Starfish Prime caused an electromagnetic pulse (EMP) that was far larger than expected, and off the scale. Researchers had found that an obvious artificial radiation belt and ionosphere was formed (Brown & Gabbe, 1963; Latter & LeLevie, 1963; Latter et al., 1961; Smith et al., 2017). The Starfish Prime electromagnetic pulse also made those effects known to the public by causing electrical damage in Hawaii, for example, setting off numerous burglar alarms, damaging a telephone company microwave link, and distorting the transmission and reception of radar waves (Vittitoe & Charles, 1989).

The majority of previous studies (e.g., Kenneth & Joe, 1974; McRary, 1971; Michael, 1971; Yee et al., 1986) on the HEMP in the ionosphere usually assumed the EMP has been excited outside of the ionosphere. These studies just simulated how the EMP wave distorted by plasmas in the ionosphere and did not involve the formation of electromagnetic pulses. This may be because previous studies (e.g., Carron & Longmire, 1976; Chadsey et al., 1975) on the X-ray-produced HEMP believed that the dominant electric field produced by X-rays in the ionosphere was the electrostatic field, which is local and cannot propagate over long distances. Thus, in the ionosphere, they just consider the propagation of the EMP generated by γ-rays outside of the ionosphere.

In this paper, we want to study the HEMP generated by X-rays in the ionosphere. Higgins et al. (1973) have proposed a method for estimating the X-ray-produced HEMP, they proposed that the photoelectrons from X-rays produce a much smaller ratio of net current to secondary ionization, and so should lead to a substantially smaller saturated $\vec{E}$. The main possibility of finding a large EMP appear to come at early time before the secondary electrons have had time to build up. However, in such a short time, the geomagnetic deflection of the photoelectrons is small, so that the transverse current is small, and only the radial electric (electrostatic) field should be considered. Based on this assumption, in this study, Higgins et al. (1973) only investigated the electrostatic field. After that, this hypothesis was widely used in subsequent research. We will test this assumption in this paper. But this study ignored the much lower air density, overestimated the number density of secondary electrons, and overestimated the number density of secondary electrons, and hence ignored the electromagnetic component. We will reexamine this issue in this study.

Since the strength of excited EMP is much higher than that of the geomagnetic field, EMP fields have a more dramatic effect on electron motion. Since excited electromagnetic fields influence electron motion and vice versa, the particle-in-cell/Monte Carlo collision (PIC/MCC) model (Birdsall, 1991; Nanbu, 1997; Nanbu & Yonemura, 1998; Vahedi & Surendra, 1995) would be an excellent tool for simulating this self-consistent operation. This is the first time that a PIC/MCC model has been used to simulate the HEMP. Because the PIC/MCC model is based on first principles, we do not need to make any additional assumptions. Therefore, it is almost the only way to test the validity of assumptions in previous work since it is impossible to do experiments on such a large scale after the nuclear test ban.

In this paper, via a PIC/MCC simulation model, we study the HEMP produced by X-rays in the ionosphere, and test the applicability of several approximations in previous studies. The study is organized as follows: the simulation model is described in Section 2, the simulation results are presented in Section 3, conclusion and summary are illustrated in Section 4.

2. Simulation Model Description

A sketch of coordinates and simulation model used in this study is presented in Figure 1. Prompt X-rays incident from the left side of the simulation domain. The simulation domain is full of air molecules (20% oxygen molecules and 80% nitrogen molecules). The geomagnetic field is represented by the out-of-plane B_z. Prompt X-rays propagate along the x axis, the geomagnetic field is along the z axis, and $x-y-z$ axes constitute right-handed coordinates. The left and right boundaries are absorbing boundaries for particles and electromagnetic fields. In our simulation code, the absorbing boundaries for particles are achieved via

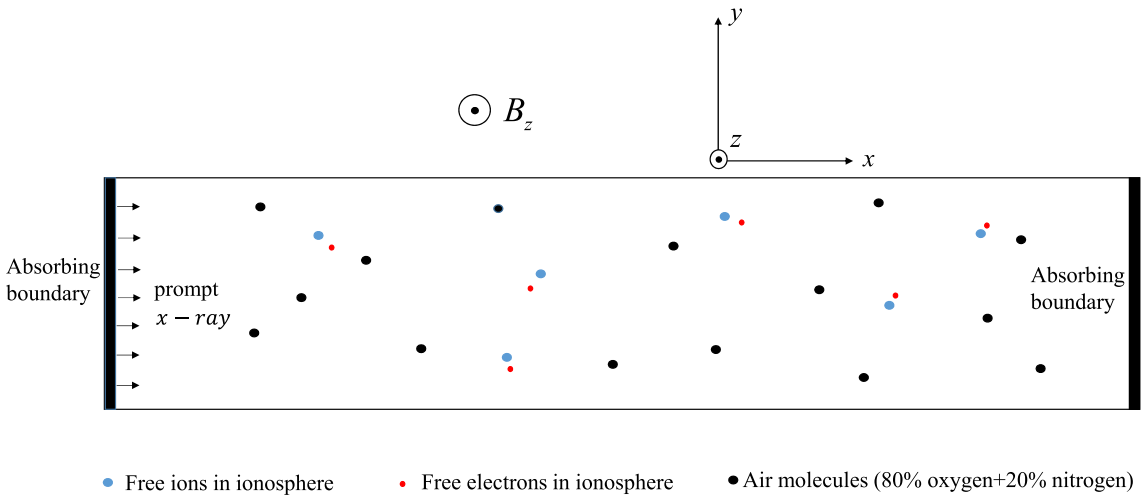

Figure 1. A sketch of the simulation model. Prompt X-rays incident from the left side of the simulation domain. The simulation domain is full of air molecules (20% oxygen molecules and 80% nitrogen molecules). The geomagnetic field is represented by the out-of-plane B_z. The X-ray propagation along the x axis, the geomagnetic field is along the z axis, and $x-y-z$ axes constitute right-handed coordinates. The left and right boundaries are absorbing boundaries for particles and electromagnetic fields.

removing particles when they cross these boundaries, the absorbing boundaries for electromagnetic waves are achieved via using perfectly matched layer (PML, Berenger, 1994), the width of this layer is five grids.

The main processes involved in the simulation are: photoelectrons are produced by X-rays via photoionization; energetic photoelectrons ionize air molecules to generate secondary electrons with average energy of tens of electron volts; secondary electrons and free electrons in the ionosphere multiply via avalanche; eventually, the motion of all of these electrons constitute current and emit electromagnetic fields. The self-consistent interaction between ions/electrons and field is described by a PIC (particle-in-cell) simulation model. The reaction between electrons and air molecules can be described with the Monte Carlo simulation model. In this study, the involved chemical processes are: the elastic collision between electrons (photoelectrons, secondary electrons, and free electrons) and nitrogen/oxygen molecules, the ionization impact between electrons and nitrogen/oxygen molecules, and two-body attachment between electrons and nitrogen molecules ($e + O_2 \rightarrow O + O^-$). The three-body attachment ($e + O_2 + M \rightarrow O_2^- + M$, where M is an additional molecule, N_2 or O_2) is neglected due to its small collision frequency compared to the two-body attachment at low pressure. The cross sections of elastic collision, ionization, and attachment between electrons and molecules are shown in Figure 2. In which, the cross section of between oxygen/nitrogen molecules is presented in Figures 2a and 2b. The low energy part ($E < 10$ keV) of Figure 2 is obtained from LXCat (https://nl.lxcat.net/data/set_type.php), and the high energy part ($E > 10$ keV) calculated using screened Rutherford cross section (Jacob, 1973).

It should be noted that the photoionization process cannot currently be simulated using a PIC/MCC simulation model. This procedure, like the commonly used in others' studies, is replaced by a process that gradually inject electrons to the simulation domain. The ionization source moving along the x axis with the light speed emits photoelectrons and ions. According to the previous study (Karzas & Latter, 1965), the Compton electrons produced by γ-rays are primarily distributed within 10° along the γ-ray propagation direction; therefore, the widely used assumption that Compton electrons all propagate along the γ-ray propagation direction is appropriate. However, owing to the large scattering angle θ (the angle between the motion direction of photoelectrons and X-rays) of photoelectrons, this assumption should not be appropriate. The angular distribution of photoelectrons is (Higgins et al., 1973, their equation 3.5.22 on the page 85):

$$f(\theta) = 0.75/\left(1 - v/c\cos\theta\right)^4\left(1 - v^2/c^2\right)^2\left(1 - \cos^2\theta\right), \quad (1)$$

where v is the mean velocity of photoelectrons and c is the speed of light in vacuum. This angular distribution is adopted in our simulation model. The run with forward-moving photoelectrons is performed to evaluate the applicability of the forward-moving assumption. The number density of photoelectrons

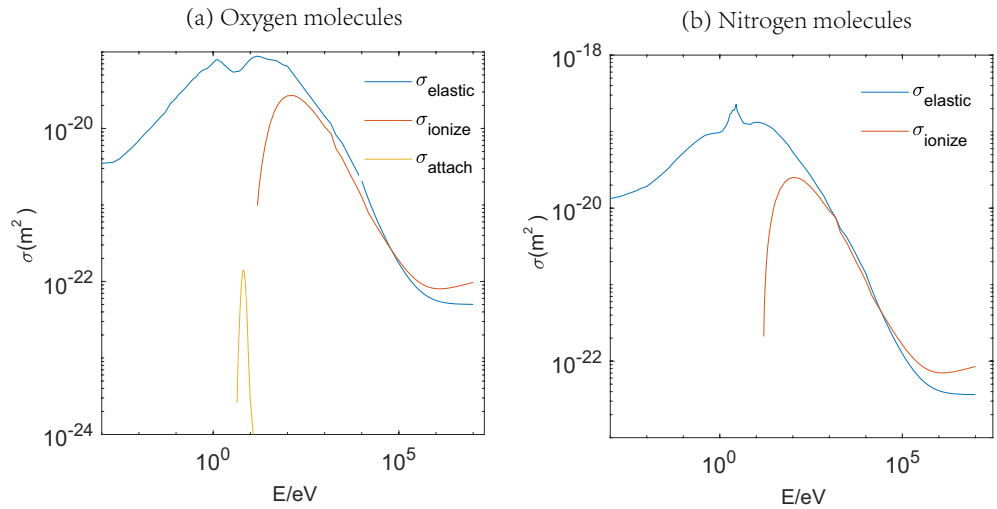

Figure 2. (a) The cross sections between electrons and oxygen molecules. (b) The cross sections between electrons and nitrogen molecules. The red, blue, and yellow lines represent ionization, elastic collision, and attachment between electrons and molecules.

produced by X-rays decreases as X-rays propagate along x axis. The number density of photoelectrons is (Karzas & Latter, 1965)

$$n\left(x,t\right) = n_0\left(\mathrm{t}\right)\exp\left(-\int dx/\lambda_X\right), \tag{2}$$

where λ_X is the mean free path of X-rays, which is roughly $\lambda_X = 1/4E_x^{1/3}\rho_0/\rho(\mathrm{cm})$, and E_x is the average energy of X-rays in kilovolts, ρ_0/ρ is the ratio of sea-level air density to the air density at the point of interest. The energy of photoelectrons is close to the energy of incident X-rays, the energy distribution of these photons should satisfy the blackbody radiation spectrum. But the computation of photoelectrons to simulate such an energy spectrum is too massive. In this paper, we assume photoelectrons are monoenergetic. The incident number density of photoelectrons $n_0(t)$ has the time history (Higgins et al., 1973)

$$n_0\left(t\right) = 2\times10^{11}\frac{a\times b}{b-a}\left(e^{-at} - e^{-bt}\right), \tag{3}$$

where $a = 1\,\mathrm{ns}^{-1}$, $b = 0.5\,\mathrm{ns}^{-1}$.

The size of each cell is limited by the condition $\Delta x < 1/3\lambda_D$, λ_D is the Debye length. The time step is limited by the condition that $\Delta x/\Delta t > c$. The length of simulation domain L is longer than λ_X. In this paper, the spatial step is $\Delta x = 0.01\,\mathrm{m}$, the time step is $\Delta t = 0.001\,\mathrm{ns}$. In the innermost layer (D-region) of the ionosphere, L is several hundred meters, which is much smaller than the characteristic length of density changes, so the constant number density approximation is appropriate. The number density of air molecules is set to be $2.5\times10^{21}\,\mathrm{m}^{-3}$, which corresponds to the number density at the altitude of 68 km (in the D-region of the ionosphere). For X-ray photons with $E_x = 10\,\mathrm{keV}$ and 20 keV, the mean free paths are $L_x = 53.8\,\mathrm{m}$ and $L_x = 67.9\,\mathrm{m}$, respectively. The length of the simulation domain is $L = 200\,\mathrm{m}$, and the total number of the grid is 20,000. According to previous studies, the number density of free ions/electrons at the altitude of 68 km is about $2\times10^9\,\mathrm{m}^{-3}$, which is significantly lower than that of secondary electrons (about $2\times10^{12}\,\mathrm{m}^{-3}$ in our simulation). Considering these two kinds of electrons play the same role, that is, constituting a conductive current and weakening the primary current. The free electrons/ions in the D-region of the ionosphere can be neglected due to their much lower number density compared with that of secondary electrons. In addition, given the high number density of secondary electrons, not only do we use the macroparticles with variable weights in the simulation, but we also combine the macroparticles when the number of macroparticles in a cell exceeds 100. In order to reduce the noise produced by the combination, two macroparticles with similar velocities will be combined.

Three runs with different parameters are performed in this study, the corresponding parameters are illustrated in Table 1. Run 1 and Run 2 are performed to illustrate the effect of photoelectrons with different

Table 1
Three Runs With Different Parameters[a]

	Photoelectrons energy (keV)	Angular distribution
Run 1	10	$f(\theta)$
Run 2	20	$f(\theta)$
Run 3	10	Forward

[a]The second column is the photoelectron energy (in keV), the third column illustrates the angular distribution of photoelectrons, $f(\theta)$ means photoelectrons are angularly distributed, and "forward" means photoelectrons only have forward velocities.

energies. Run 3 is performed to evaluate whether the assumption of forward-moving photoelectrons is appropriate.

3. Simulation Results

In this section, we will investigate the effects of photoelectrons with different energies and direction angle distributions on the HEMP, respectively.

3.1. The Effect of Photoelectron Energy on the HEMP

The effect of photoelectrons with different energies on the HEMP is illustrated in this section. As proved by the previous study (Savage et al., 2010), the electrostatic component is the electric field in the direction of X-rays propagation (i.e., E_x in our study), and the electromagnetic component is the electric field in the direction perpendicular to the X-rays propagation and geomagnetic field (i.e., E_y in our study). The electrostatic component is the local field and could not propagate. Because of the coordinated phasing effect, the electromagnetic component increases in propagation and gradually becomes the HEMP.

The history of the amplitude of these two electric field components is shown in Figure 3. Red and black lines in Figure 3 are the waveform of Run 1 and Run 2, respectively. The electrostatic component (E_x) is represented by solid lines, the electromagnetic component (E_y) is illustrated by dashed lines. The amplitude of the electrostatic component (E_x) quickly increases to the peak within 50 ns, and then decreases gradually. The amplitude of electromagnetic field component (E_y) gradually increases and reaches saturation. Previous studies (e.g., Carron & Longmire, 1976; Chadsey et al., 1975; Higgins et al., 1973) proposed that the amplitude of the electromagnetic field component is smaller than that electrostatic component. Thus, in their work, they only considered the electrostatic component. However, as shown in Figure 3, this assumption is only valid for the stage of $t < 50$ ns, during which E_x is an order of magnitude greater than E_y. Following that, E_x decreases while E_y increases gradually, these two values will be equal at $t \sim 300$ ns. This assumption is no longer appropriate throughout this period.

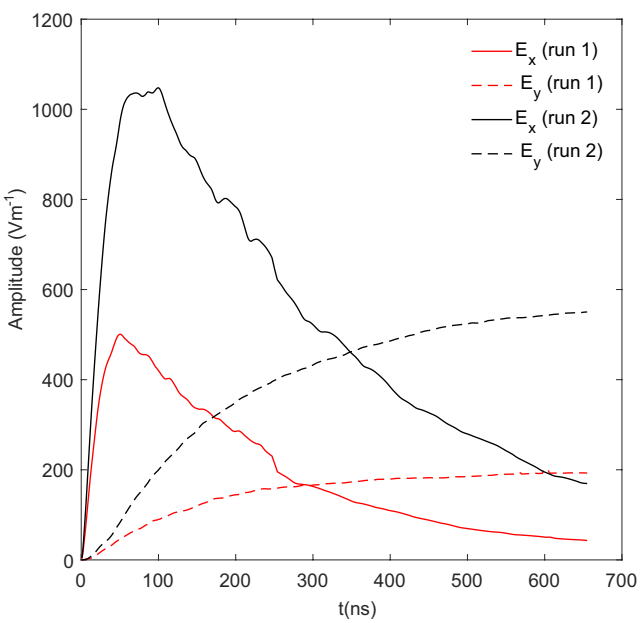

Figure 3. The evolution of the maximum amplitudes of the electrostatic field E_x (represented by solid lines) and the electromagnetic field E_y (represented by dashed lines). Red and black lines represent the field in the Runs 1 and 2, respectively.

The amplitudes of electric fields are also closely related to the average energy of photoelectrons. The maximum amplitude of the electrostatic component E_x for Run 2 with photoelectrons energy $E_x = 20$ keV is about 1,050 V/m, nearly twice that for Run 1 with photoelectrons energy $E_x = 10$ keV. Similar result can be found in the electromagnetic component E_y. The saturated amplitude of E_y is the consequence of a competition between the primary electron current and the secondary electron current. Larger photoelectron energy results in a longer saturation time, which eventually results in a larger saturation amplitude.

The waveform of electric fields at different observed points is shown in Figure 4. The red and black lines represent the waveforms of Runs 1 and 2, respectively. We have subtracted the delay time (the time it takes for X-rays to travel from the left side of the simulation domain to the observation point) in different figures to make comparison more convenience. The amplitude of the electrostatic field E_x is larger than that of the electromagnetic field E_y for the observer located at small x. As the observation position x increases, the amplitude of E_x decreases while the amplitude of E_y increase. When observer locates at large x, the amplitude of the electrostatic field E_x will be smaller than that of electromagnetic field E_y. This is consistent with the result illustrated in Figure 3. As shown in Figures 4a and 4b, at the position $x = 15$ m, the amplitude of E_x is much larger than that of E_y. At $x = 96$ m (shown in Figure 4c), the amplitude of E_x is close to that of E_y. With the further increase of observation position x, at $x = 144$ m (shown in Figure 4c), the amplitude of E_y

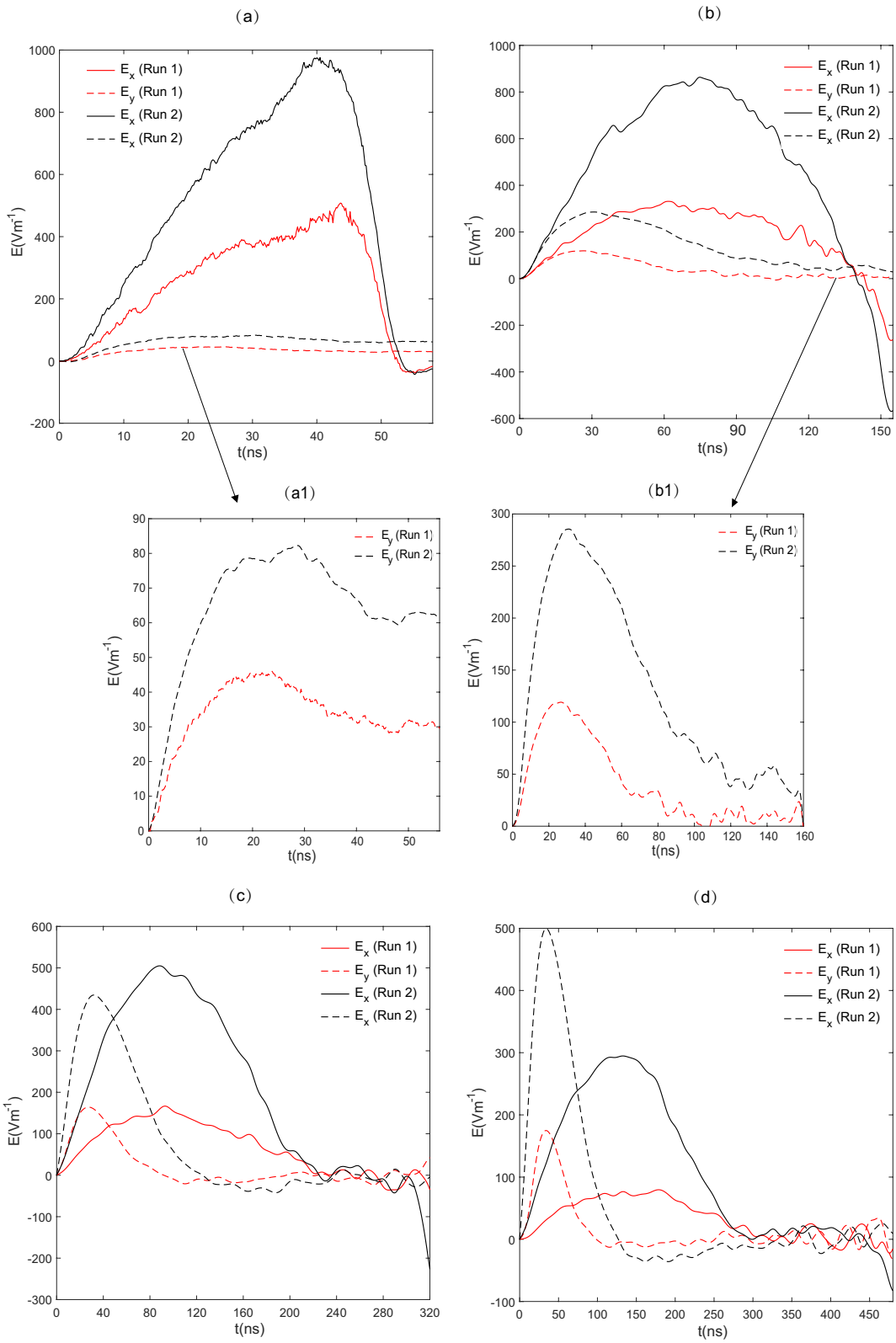

Figure 4.

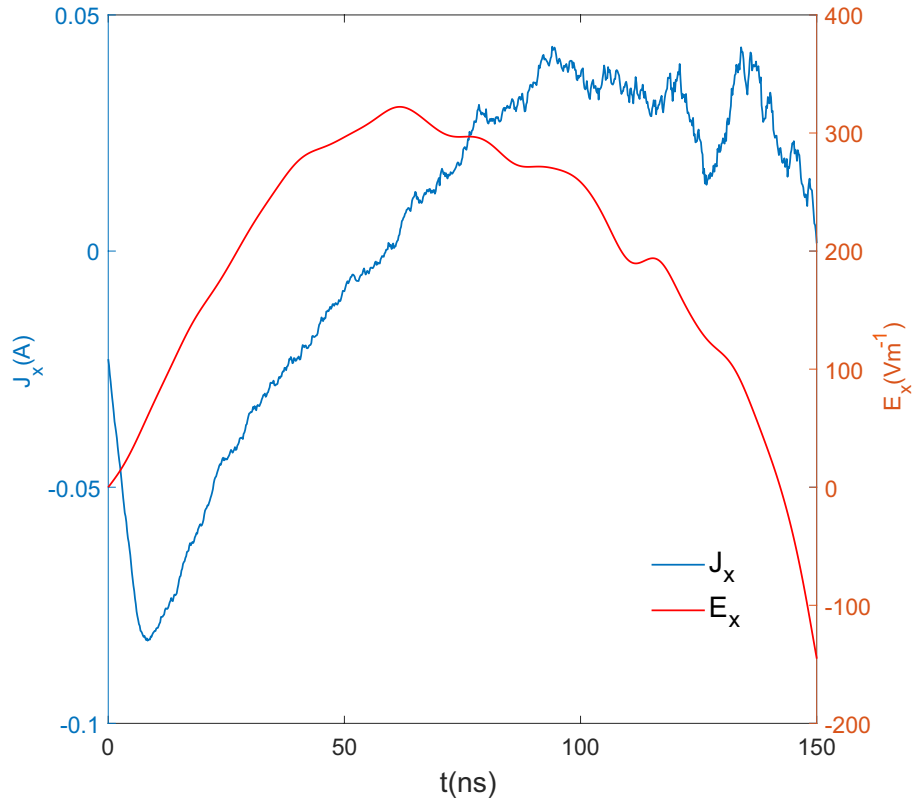

Figure 5. The waveforms of J_x (ordinates on the left) and E_x (ordinates on the right) for the observation point located at $x = 45$ m in Run 1.

will be larger than that of E_x. The waveform of E_y (dashed lines) is the standard E1 HEMP waveform (Hoad & Radasky, 2013), the rising time is about 30 ns.

It should be noted that the tail of the waveform of E_x is less than zero, which is caused by the reverse current at the tail. Figure 5 depicts the waveforms of E_x and J_x for Run 1. According to the electrostatic field E_x equation: $\varepsilon_0 \frac{\partial E_x}{\partial t} = -J_x$, the positive (negative) J_x will result in decreasing (increasing) the amplitude of the positive E_x or increasing (decreasing) of the amplitude of the negative E_x. As a result, the maximum E_x corresponds to the point with $J_x = 0$, and the positive J_x reduces the amplitude of the positive E_x until $E_x < 0$, and then increase the amplitude of negative E_x.

In conclusion, previous study ignored the influence of air density, and overestimated the number density of secondary electrons. As a result, the saturation time is underestimated, resulting in an underestimate of the electromagnetic component. In fact, the electromagnetic component can actually rise to an order of magnitude with the electrostatic component and should be considered. Because the electromagnetic component has a larger range of action and has a significant influence on the safety of adjacent spacecraft, our study is critical to assessing aircraft flight safety.

Figure 4. The waveform of the electric field at different observed points. Observation points are located at (a) $x = 15$ m, (b) $x = 45$ m, (c) $x = 96$ m, and (d) $x = 144$ m, respectively. (a1) and (b1) are enlarged views of (a) and (b), respectively. Only the electromagnetic component E_y is presented in (a1) and (b1). The red and black lines represent the waveforms of Runs 1 and 2, respectively. The electrostatic component (E_x) is shown with solid lines, while the electromagnetic component (E_y) is shown with dotted lines. The electrostatic component (E_x) is shown with solid lines, while the electromagnetic component (E_y) is shown with dotted lines.

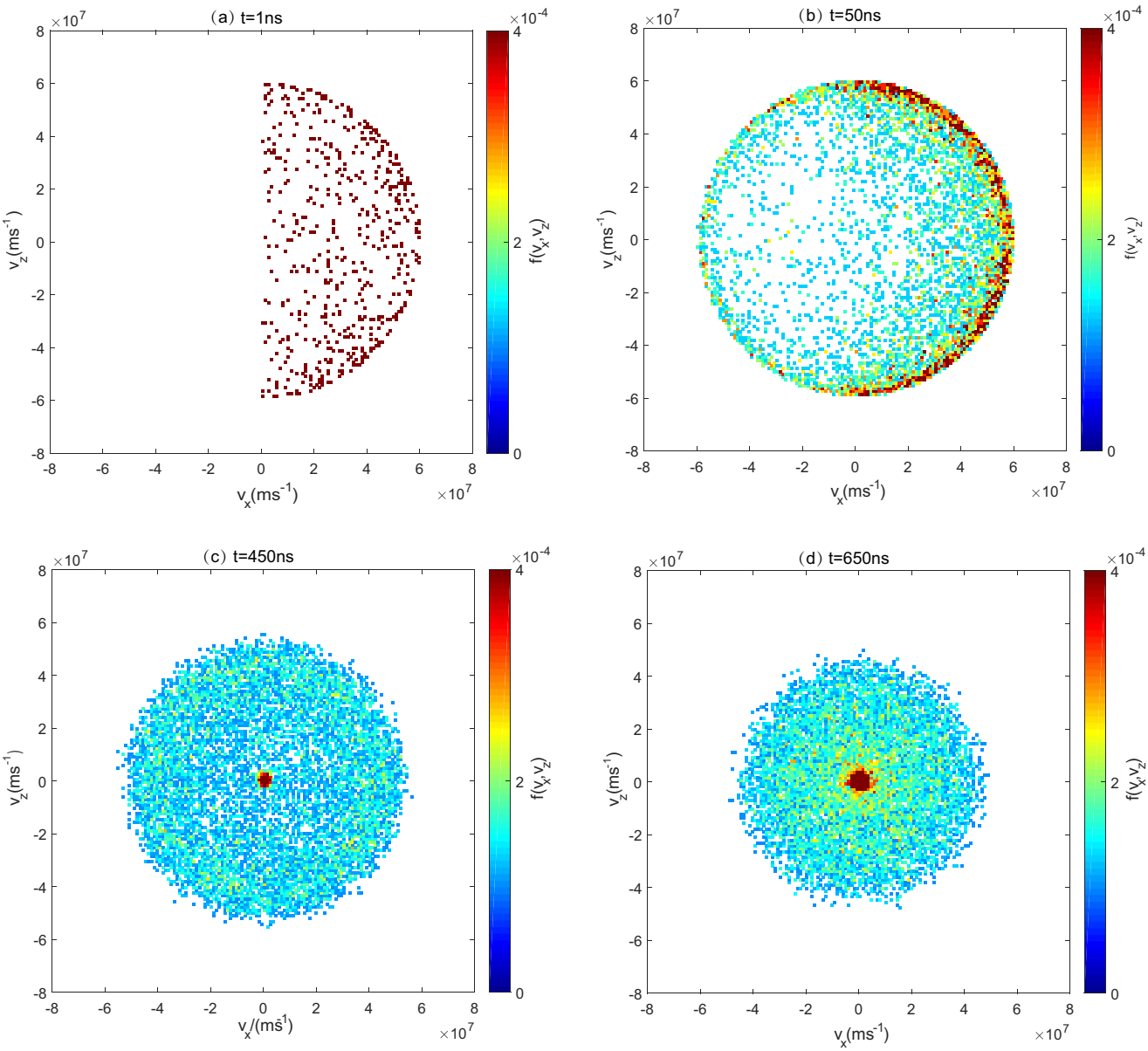

Figure 6. The evolution of photoelectrons distribution in the $v_x - v_z$ plane for Run 1 at different moments (a) $t = 1$ ns, (b) $t = 50$ ns, (c) $t = 450$ ns, and (d) $t = 650$ ns.

3.2. The Evolutions of Photoelectrons and Secondary Electrons

The kinetics of photoelectrons and secondary electrons are critical for interpreting the HEMP process. We will discuss the evolution of electrons in this subsection. In the following, we will study the dynamic evolution process of primary electrons and secondary electrons, respectively.

The evolution of primary electrons in the in the $v_x - v_z$ plane for Run 1 is shown in Figure 6. Primary electrons are significantly slowed. The initial distribution of primary electrons is shown in Figure 6a, photoelectrons are distributed in the right semicircle plane. Due to the Lorentz force and elastic collisions, as shown in Figure 6b, photoelectrons are gradually transported to the whole plane. Simultaneously, the primary electrons are considerably slowed, and a huge number of electrons congregate near $v_x = 0$. This can be further illustrated by the evolution of photoelectrons in the phase space $x - v_x$ presented in Figure 7. Initially, photoelectrons only disperse in the space $v_x > 0$ (as shown in Figure 7a). Subsequently, with X-rays propagating to the right side, photoelectrons continue to be injected into the phase space. As shown in Figure 7b,

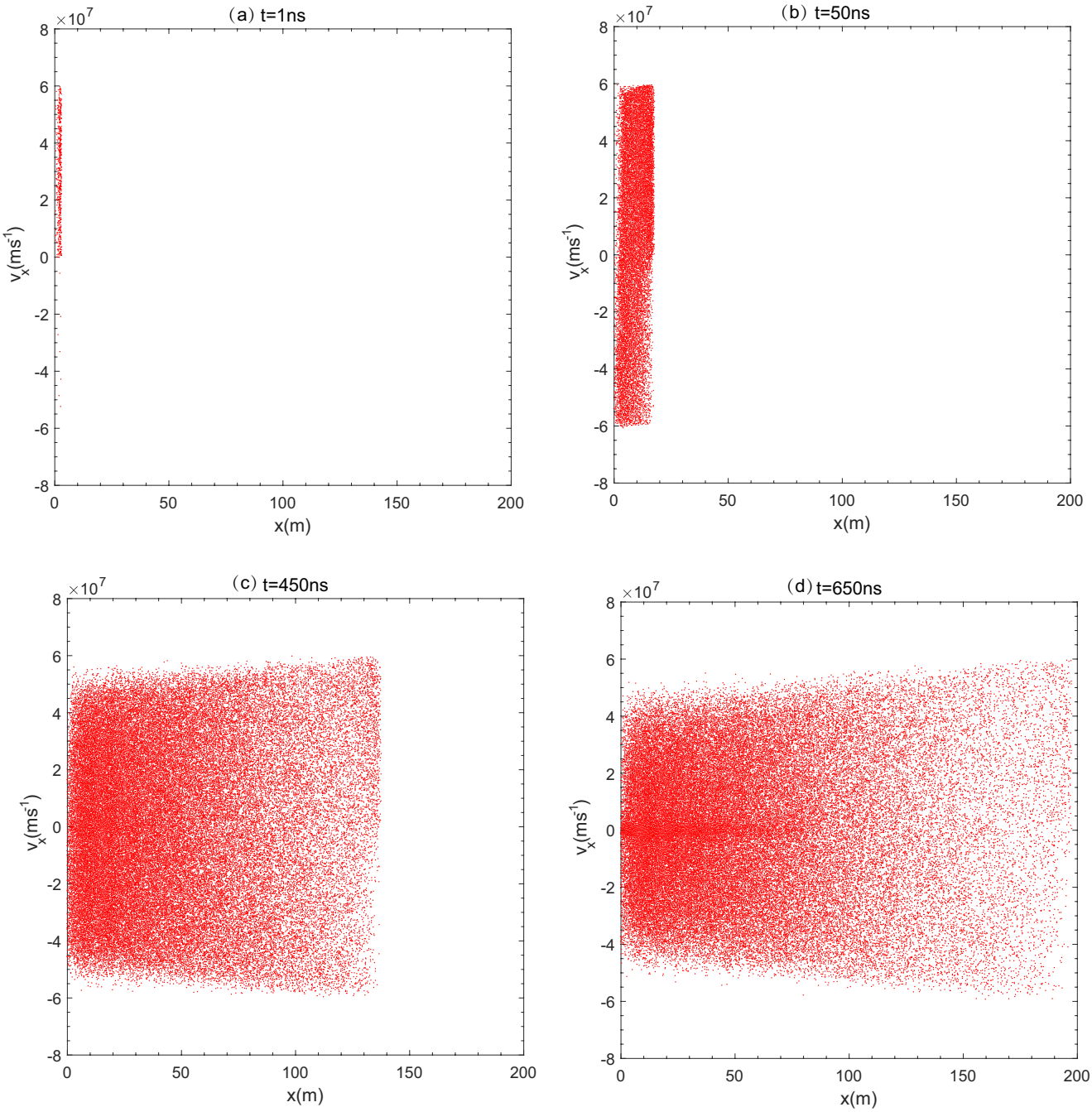

Figure 7. The evolution of the distribution of photoelectrons in the phase space ($x - v_x$ plane) for Run 1 at different moments (a) $t = 1$ ns, (b) $t = 50$ ns, (c) $t = 450$ ns, and (d) $t = 650$ ns.

due to the Lorentz force and elastic collisions, photoelectrons are transported to the plane with $v_x < 0$. In Figures 7c and 7d, the number density of photoelectrons with $v_x \sim 0$ in the left side increases significantly. This implies that a significant number of photoelectrons ejected at the early stage are decreased to $v_x \sim 0$.

The distribution of secondary electrons is critical to determining the conductivity, which directly affects the saturated amplitude of the HEMP. The distribution of secondary electrons in Run 1 at the early stage is presented in Figure 8. The distribution of "newly born" secondary electrons produced via ionization deviates away from the Maxwellian (or drifting Maxwellian) distribution. Through elastic collision, these electrons will gradually reach an equilibrium state, and correspondingly, their distribution function will gradually

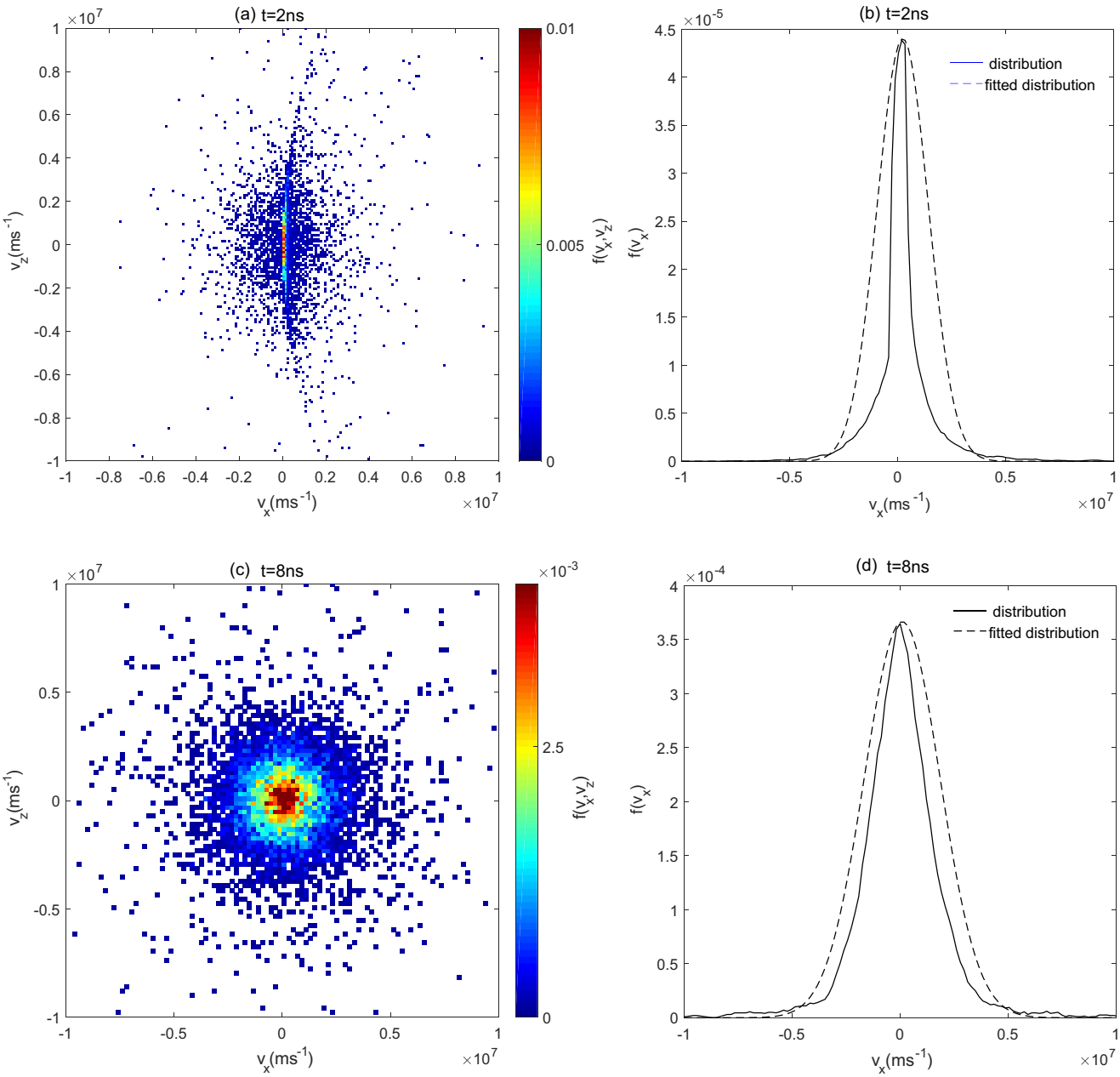

Figure 8. (a) The distribution of secondary electrons for Run 1 at $t = 2$ ns in $v_x - v_z$ plane. (b) The distribution of secondary electrons $f(v_x)$ for Run 1 at $t = 2$ ns (represented by solid line), the dashed line is the distribution fitted by the Maxwellian distribution. (c) The distribution of secondary electrons for Run 1 at $t = 8$ ns in $v_x - v_z$ plane. (d) The distribution of secondary electrons $f(v_x)$ for Run 1 at $t = 8$ ns (represented by solid line), the dashed line is the distribution fitted by the Maxwellian distribution.

trend to the Maxwellian (or drifting Maxwellian) distribution. As illustrated in Figure 8a, at $t = 2$ ns, "newly born" secondary electrons deviate significantly from equilibrium Maxwellian distribution, v_z is much larger than v_x. This indicates that the scattering angle ($\theta = \arctan(v_z/v_x)$) of these electrons approaches 90°. This phenomenon can be explained by the scattering angles of secondary electrons after ionization, the scattering angles of secondary electrons (χ_{se}) and scattered preliminary electrons (χ_{sc}) are presented in the following:

$$\cos\chi_{se} = \left(\frac{\varepsilon_{se}}{\varepsilon_{inc} - \varepsilon_{io}}\right)^{0.5}, \tag{4}$$

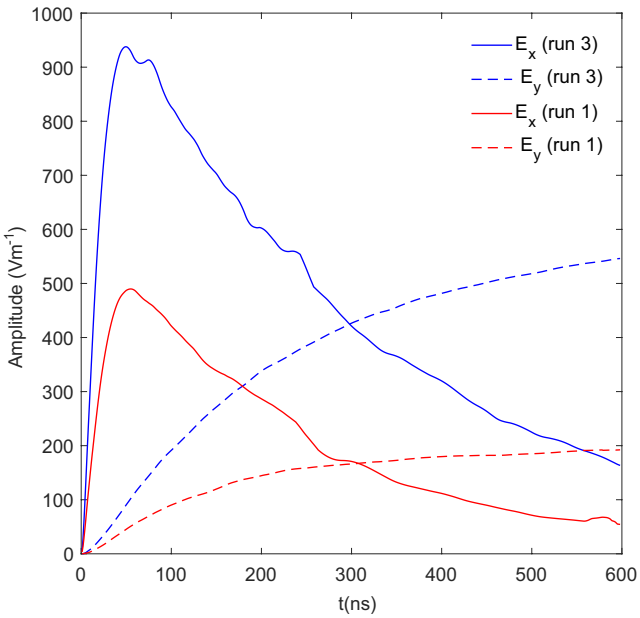

Figure 9. The evolution of the amplitude of E_x and E_y for Run 1 and Run 3.

$$\cos\chi_{sc} = \left(\frac{\varepsilon_{sc}}{\varepsilon_{inc} - \varepsilon_{io}}\right)^{0.5}, \tag{5}$$

in which, ε_{inc} and $\varepsilon_{\mathrm{sec}}$ are the energies of the incident electrons and secondary electrons, respectively, ε_{io} is the ionization energy. According to Equations 4 and 5, $\cos^2\chi_{sc} + \cos^2\chi_{se} = 1$, thus $\chi_{sc} + \chi_{se} = 90^{\circ}$, this means the scattering angles of secondary and scattered electrons satisfy momentum conservation. In the simulation, the initial energy of the incident primary electron is $\varepsilon_{inc} = 10$ KeV, the ionization energy threshold $\varepsilon_{i0} = 15.6$ eV for nitrogen and 12.5 eV for oxygen molecules. In general, the secondary electrons generated via ionization by primary electron has much lower energy than ε_{inc}, that is, $\varepsilon_{\mathrm{sec}} \ll \varepsilon_{inc}$, thus, $\cos\chi_{\mathrm{sec}} \ll 1$, hence $\chi_{\mathrm{sec}} \to 90^{\circ}$. This indicates that when the energy of incident electron ε_{inc} is much larger than the ionization threshold ε_{io}, the trajectory of incident electron remains unchanged, that is, $\chi_{sc} \sim 0$, while secondary electrons are perpendicularly scattered.

The non-Maxwellian distribution of secondary electrons can be better illustrated in Figure 8b, where the solid line represents the distribution $f(v_x)$ of secondary electrons at $t = 2$ ns, the dashed line represents the fitted Maxwellian distribution. The fitted Maxwellian distribution is obtained by substituting the mean velocity v_d, temperature $kT = 0.5m_e(v_x - v_d)^2$, and amplitude A, into the drifting Maxwellian distribution function $f(v_x) = A\exp[m_i(v_x - v_d)^2/kT]$. The solid line deviates significantly from the dashed line, indicating that the distribution of the secondary electrons at $t = 2$ ns is far from Maxwellian distribution. Subsequently, as shown in Figures 8c and 8d, via frequent elastic collisions, at $t = 8$ ns, secondary electrons approaches Maxwellian distribution.

In conclusion, the "swarm theory" (Higgins et al., 1973; Pusateri et al., 2015, 2016), which is based on the drifting Maxwellian distribution, could not be applied to describe the motion of secondary electrons ionized by photoelectrons before 8ns. This is consistent with results in a recent experiment (Gilbert et al., 2013).

3.3. The Effect of Photoelectron Angle Distribution on the HEMP

In addition to photoelectrons' energy, the distribution angle of photoelectrons influences HEMP. We discuss this issue in this part.

The assumption that primary electrons move forward has been widely used in previous study of the γ-ray-produced HEMP, and proved to have little effect on the peak value and the rising edge of HEMP (Li et al., 2020), this assumption has also been applied by previous studies to investigate the X-ray-produced HEMP (e.g., Carron & Longmire, 1976; Higgins et al., 1973). In this part, via comparing Run 1 and Run 3, we will study whether this assumption is appropriate for the X-ray-produced HEMP. The evolution of the amplitude of E_x and E_y for Run 1 and Run 3 is illustrated in Figure 9. In which, red and blue lines represent electric fields for Run 1 and Run 3, respectively. The electrostatic and electromagnetic fields are presented with solid and dashed lines, respectively. It is clear that E_x and E_y for Run 3 are roughly twice as large as those for Run 1. This means the assumption that photoelectrons all move forward increases the strength of electric fields significantly.

Further investigation of secondary electrons distribution reveals that secondary electrons ionized by forward-moving photoelectrons are also far from Maxwellian distribution, and need more time to reach equilibrium. As shown in Figure 10a, at $t = 8$ ns, the secondary electrons have not yet reached the equilibrium state, correspondingly, the secondary electrons in Figure 6c have achieved the equilibrium state at $t = 8$ ns. It needs to take 30 ns to reach equilibrium for forward-moving photoelectrons.

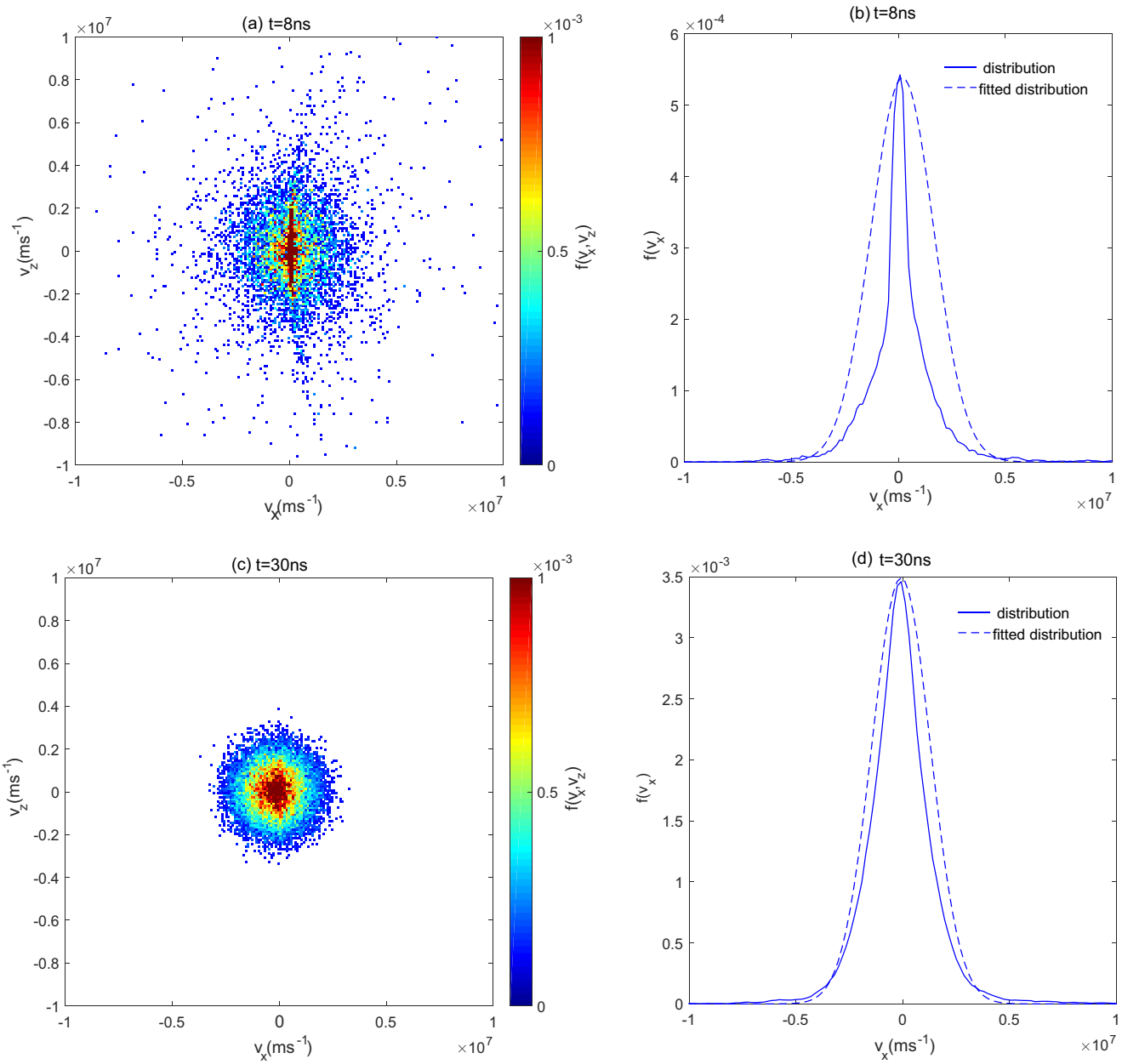

Figure 10. (a) The distribution of secondary electrons for Run 3 at $t = 8$ ns in $v_x - v_z$ plane. (b) The distribution of secondary electrons $f(v_x)$ for Run 3 at $t = 8$ ns (represented by solid line), the dashed line is the fitted Maxwellian distribution. (c) The distribution of secondary electrons for Run 3 at $t = 30$ ns in $v_x - v_z$ plane. (d) The distribution of secondary electrons $f(v_x)$ for Run 3 at $t = 30$ ns (represented by solid line), the dashed line is the distribution fitted by the Maxwellian distribution.

In conclusion, the assumption that photoelectrons move forward will lead to "newly born" secondary electrons need more time to achieve equilibrium, reducing the conductivity at the early stage and increasing the amplitude of HEMP according to the previous study (Gilbert et al., 2013). Therefore, the assumption that primary electrons move forward will cause the calculated field strength to be larger.

4. Conclusion and Summary

In this study, via a 1-D PIC/MCC simulation model, we study the HEMP produced by X-rays in the D-region of the ionosphere. We find that the amplitude of the electrostatic component (E_x) quickly increases to the peak within 50 ns, and then decreases gradually. The amplitude of electromagnetic field component (E_y) gradually increases and reaches saturation. Before $t \sim 300$ ns, the intensity of E_x is stronger than that of E_y, after that, E_y will have a stronger intensity. This is because the electromagnetic field accumulates in the propagation due to the synchronized phasing effect. This contradicts the assumption used in previous studies: E_y is much smaller than E_x, and E_y can be neglected. This is because previous scholars neglected the low air density at the altitude where the HEMP produced by X-rays, the ratio of net current to secondary ionized current has been seriously underestimated. Therefore, the saturated electromagnetic field component neglected by previous study should be considered.

The investigation of the evolution of secondary electrons produced by photoelectrons via ionization reveals an interesting phenomenon: initially, the distribution of "newly born" secondary electrons deviates away from the Maxwellian distribution. Subsequently, via frequent elastic collision, they reach equilibrium. This finding is consistent with recent experiments on secondary electrons formed by Compton electrons (Gilbert et al., 2013), which show that "newly born" secondary electrons require several ns to achieve equilibrium, rendering the "swarm hypothesis" based on the assumption that secondary electrons satisfy a drifting Maxwellian distribution invalid.

This paper also tests the widely accepted assumption that primary electrons travel forward in previous studies of the γ-ray-produced HEMP. We find that this assumption increases the strength of electric fields significantly. What's more, under this assumption, "newly born" secondary electrons need more time to achieve equilibrium, reducing the conductivity at the early stage and increasing the amplitude of HEMP (Gilbert et al., 2013). We also investigate the impact of photoelectrons' energy, the greater the photoelectron energy, the greater the maximum amplitude of HEMP.

Our study indicates that the ignored electromagnetic field in previous study (Higgins et al., 1973) should be considered. Because the electromagnetic field's impact range is significantly greater than that of the electrostatic field, the electromagnetic field of X-ray-produced HEMP is important to the flight safety of adjacent space vehicles. Besides, our simulation shows that the "newly born" secondary electrons deviate from the drifting Maxwellian distribution, thus fluid equations cannot be applied to describe the motion of these electrons. Recent experiment also revealed this point. Compared with earlier nuclear explosion experiments, for example, the Starfish prime, we found that the unexpectedly large EMP is caused by the synchronized phasing effect. The distortion of the radar waves is caused by an increase of local electron density, especially secondary electron density. Our simulation work has Deepened the understanding of these phenomena.

Data Availability Statement

The simulation data and code will be preserved on Jiansheng Yao et al. (2021). Nuclear high-altitude electromagnetic pulse (HEMP): X_ray_HEMP_JGR_paper, 10.5281/zenodo.5565558.

Acknowledgments
This work was supported by the National Science Foundation of China (11822401).

References

Berenger, J. (1994). A perfectly matched layer for the absorption of electromagnetic waves. *Journal of Computational Physics*, *114*(2), 185–200. https://doi.org/10.1006/jcph.1994.1159

Berthold, W. K., Harris, A. K., & Hope, H. J. (1960). Worldwide effects of hydromagnetic waves due to Argus. *Journal of Geophysical Research*, *65*, 2233–2239. https://doi.org/10.1029/JZ065i008p02233

Birdsall, C. K. (1991). Particle-in-cell charged-particle simulations, plus Monte Carlo collisions with neutral atoms, PIC-MCC. *IEEE Transactions on Plasma Science*, *19*(2), 65–85. https://doi.org/10.1109/27.106800

Bomke, H. A., Baiton, I. A., Grote, H. H., & Harris, A. K. (1964). Near and distant observations of the 1962 Johnston Island high-altitude nuclear tests. *Journal of Geophysical Research*, *69*, 3125–3136. https://doi.org/10.1029/JZ069i015p03125

Bomke, H. A., Ramm, W. J., Goldblatt, S., & Klemas, V. (1960). Global hydromagnetic wave ducts in the exosphere. *Nature*, *185*, 299–300. https://doi.org/10.1038/185299a0

Brown, W. L., & Gabbe, J. D. (1963). The electron distribution in the Earth's radiation belts during July 1962 as measured by Telstar. *Journal of Geophysical Research*, *68*, 607–618. https://doi.org/10.1029/JZ068i003p00607

Carron, N. J., & Longmire, C. L. (1976). Electromagnetic pulse produced by obliquely incident X rays. *IEEE Transactions on Nuclear Science*, *23*(6), 1897–1902. https://doi.org/10.1109/tns.1976.4328596

Casaverde, M., Giesecke, A., & Cohen, R. (1963). Effects of the nuclear explosion over Johnston Island observed in Peru on July 9, 1962. *Journal of Geophysical Research*, *68*, 2603–2611. https://doi.org/10.1029/JZ068i009p02603

Chadsey, W. L., Wilson, C. W., & Pine, V. W. (1975). X-ray photoemission calculations. *IEEE Transactions on Nuclear Science*, *22*(6), 2345–2350. https://doi.org/10.1109/tns.1975.4328131

Cotterman, R. W. (1965). Electromagnetic detection of nuclear explosions. *IEEE Transactions on Nuclear Science*, *12*, 99–103. https://doi.org/10.1109/tns.1965.4323572

Crook, G. M., Greenstadt, E. W., & Inouye, G. T. (1963). Distant electromagnetic observations of the high-altitude nuclear detonation of July 9, 1962. *Journal of Geophysical Research*, *68*, 1781–1784. https://doi.org/10.1029/JZ068i006p01781

Dinger, H. E., & Garner, W. E. (1963). Whistler observations in connection with nuclear explosions. *Journal of Geophysical Research*, *68*, 5641–5648. https://doi.org/10.1029/JZ068i020p05641

Field, E. C., & Greifinger, C. (1967). Geomagnetic fluctuations due to impulse sources with applications to high-altitude nuclear bursts. *Journal of Geophysical Research*, *72*, 317–329. https://doi.org/10.1029/JZ072i001p00317

Gilbert, J. L., Radasky, W. A., & Savage, E. R. (2013). Study of nonequilibrium air chemistry. *IEEE Transactions on Electromagnetic Compatibility*, *55*(3), 446–450. https://doi.org/10.1109/temc.2013.2243839

Hess, W. N. (1964). *The effects of high altitude explosions (PDF) (Technical report NASA TN D-2402)*. National Aeronautics and Space Administration.

Higgins, D. F., Longmire, C. L., & O'Dell, A. A. (1973). *A method for estimating the X-ray produced electromagnetic pulse observed in the source region of a high-altitude burst*. Mission Research Corp Santa Barbara Calif. Retrieved from https://apps.dtic.mil/sti/citations/AD0774152

Hoad, R., & Radasky, W. A. (2013). Progress in high-altitude electromagnetic pulse (HEMP) standardization. *IEEE Transactions on Electromagnetic Compatibility*, *55*(3), 532–538. https://doi.org/10.1109/temc.2012.2234753

Hoerlin, H. (1976). *United States high-altitude test experiences: A review emphasizing the impact on the environment*. Los Alamos Scientific Laboratory. https://doi.org/10.2172/7122163

Jacob, J. H. (1973). Multiple electron scattering through a slab. *Physical Review A*, *8*(1), 226–235. https://doi.org/10.1103/physreva.8.226

Jones, C. B., Doyle, M. K., Berkhouse, L. H., Calhoun, F. S., & Martin, E. J. (1982). *Operation Argus: 1958* (technical report DNA 6039F). Defense Nuclear Agency.

Karzas, W. J., & Latter, R. (1965). Detection of the electromagnetic radiation from nuclear explosions in space. *Physical Review*, *137*(5B), B1369–B1378. https://doi.org/10.1103/physrev.137.b1369

Kenneth, C. C., & Joe, M. (1974). *EMP propagation in the ionosphere, EMP Theoretical Notes 192*. Air Force Weapons Laboratory and Dikewood Corp. Retrieved from http://ece-research.unm.edu/summa/notes/TheoreticalPDFs/TN192.pdf

Latter, R., Herbst, R. F., & Watson, K. M. (1961). Detection of nuclear explosions. *Annual Review of Nuclear Science*, *11*, 371–418. https://doi.org/10.1146/annurev.ns.11.120161.002103

Latter, R., & LeLevier, R. E. (1963). Detection of ionization effects from nuclear explosions in space. *Journal of Geophysical Research*, *68*, 1643–1666. https://doi.org/10.1029/JZ068i006p01643

Leuthiiuser, K. D. (1992). *A complete EMP environment generated by high-altitude nuclear bursts* (pp. 20). Retrieved from http://ece-research.unm.edu/summa/notes/TheoreticalPDFs/TN363.pdf

Li, Y., Wang, J., Zuo, Y., Zhu, J., & Fan, R. (2020). Simulation of high-altitude nuclear electromagnetic pulse using a modified model of scattered gamma. *IEEE Transactions on Nuclear Science*, *67*(12), 2474–2480. https://doi.org/10.1109/tns.2020.3031320

Longmire, C. L. (1978). On the electromagnetic pulse produced by nuclear explosions. *IEEE Transactions on Electromagnetic Compatibility*, *26*(1), 3–13. https://doi.org/10.1109/temc.1978.303688

Maraschi, L., & Cavaliere, A. (1977). X-ray bursts of nuclear origin. In *Highlights of astronomy* (pp. 127–128). Springer. https://doi.org/10.1007/978-94-010-1248-5_12

McRary, J. (1971). Amplitude distribution of an electromagnetic pulse propagated through the atmosphere. *IEEE Transactions on Antennas and Propagation*, *19*(1), 155–156. https://doi.org/10.1109/tap.1971.1139891

Meng, C. (2013). Numerical simulation of the HEMP environment. *IEEE Transactions on Electromagnetic Compatibility*, *55*(3), 440–445. https://doi.org/10.1109/temc.2013.2258024

Michael, A. M. (1971). *A standard ionosphere for the study of EMP propagation (EMP Theoretical Notes 117)*. Retrieved from http://ece-research.unm.edu/summa/notes/TheoreticalPDFs/TN117.pdf

Nanbu, K. (1997). Momentum relaxation of a charged particle by small-angle Coulomb collisions. *Physical Review E*, *56*(6), 7314–7314. https://doi.org/10.1103/physreve.56.7314

Nanbu, K., & Yonemura, S. (1998). Weighted particles in Coulomb collision simulations based on the theory of a cumulative scattering angle. *Journal of Computational Physics*, *145*(2), 639–654. https://doi.org/10.1006/jcph.1998.6049

Price, G. H. (1974). The electromagnetic pulse from nuclear detonations. *Reviews of Geophysics*, *12*, 389–400. https://doi.org/10.1029/RG012i003p00389

Pusateri, E. N., Morris, H. E., Nelson, E., & Ji, W. (2016). Comparison of equilibrium ohmic and nonequilibrium swarm models for monitoring conduction electron evolution in high-altitude EMP calculations. *Journal of Geophysical Research: Atmospheres*, *121*, 11884–11889. https://doi.org/10.1002/2016JD024970

Pusateri, E. N., Morris, H. E., Nelson, E. M., & Ji, W. (2015). Determination of equilibrium electron temperature and times using an electron swarm model with BOLSIG+ calculated collision frequencies and rate coefficients. *Journal of Geophysical Research: Atmospheres*, *120*, 7300–7315. https://doi.org/10.1002/2015JD023100

Roussel-Dupré, R. (2017). Hydroflash: A 2-D nuclear emp code founded on finite volume techniques. *Advanced Electromagnetics*, *6*(2), 14–25. https://doi.org/10.7716/aem.v6i2.472

Savage, E., Gilbert, J., & Radasky, W. (2010). *The early time (E1) high-altitude electromagnetic pulse (HEMP) and its impact on the US power gridReport Meta-R-320 for*. Oak Ridge National Laboratory. Retrieved from http://large.stanford.edu/courses/2019/ph241/rogers1/docs/meta-r-320.pdf

Smith, D., Collins, P., Fee, J., Petrosky, J. C., Terzuoli, A., & Yardim, C. (2017). Artificial ionospheric scintillation effects on communication signals in the V and W bands. In *International Applied Computational Electromagnetics Society Symposium-Italy (ACES)* (pp. 1–2). IEEE. https://doi.org/10.23919/ropaces.2017.7916366

Vahedi, V., & Surendra, M. (1995). Monte Carlo collision model for the particle-in-cell method: Applications to argon and oxygen discharges. *Computer Physics Communications*, *87*(1–2), 179–198. https://doi.org/10.1016/0010-4655(94)00171-w

Vittitoe, & Charles, N. (1989). *Did high-altitude EMP cause the Hawaiian streetlight incident? (Report)*. Sandia National Laboratories. Retrieved from http://ece-research.unm.edu/summa/notes/SDAN/0031.pdf

Wittwer, L. A., Canavan, G. H., & Brau, J. E. (1974). *Chemp: A code for calculation of high-altitude EMP*. Air Force Weapons Lab Kirtland AFB N MEX. Retrieved from http://ece-research.unm.edu/summa/notes/TheoreticalPDFs/TN198.pdf

Yee, J. H., Alvarez, R. A., Mayhall, D. J., Byrne, D. P., & DeGroot, J. (1986). Theory of intense electromagnetic pulse propagation through the atmosphere. *The Physics of Fluids*, *29*(4), 1238–1244. https://doi.org/10.1063/1.865872

Zak, A. (2006). The K project: Soviet nuclear tests in space. *The Nonproliferation Review*, *13*(1), 143–150. https://doi.org/10.1080/10736700600861418

Zhang, J., & Zhang, Y. R. (2018). Using a second-order integral equation method to study the high-altitude nuclear emp. *IEEE Transactions on Electromagnetic Compatibility*, *61*(5), 1483–1491.